ADVANCED ENERGY MATERIALS
www.advenergymat.de

Revealing Dynamic Evolution of the Anode-Electrolyte Interphase in All-Solid-State Batteries with Excellent Cyclability

*Se Young Kim, Seong-Min Bak, KyuJung Jun, Gerbrand Ceder, and Guoying Chen**

All-solid-state-batteries (ASSBs) based on a halide solid electrolyte (SE) and a lithium-metal based anode typically have poor cyclability without a buffer layer (such as Li_3PS_4 or Li_6PS_5Cl) to prevent the degradation reactions. Here excellent cycling stability of ASSB consisting of an uncoated single-crystal $LiNi_{0.8}Co_{0.1}Mn_{0.1}O_2$ cathode and a Li_3YCl_6 (LYC) SE separator in direct contact with a Li-In anode are demonstrated. Through a combination of electrochemical measurements, synchrotron micro-X-ray absorption and diffraction analyses, and density functional theory calculations, reveal for the first time that along with the standard Li^+ transport during charge/discharge, indium in the Li-In anode also participates in the redox reactions. The in-situ generated In^{3+} preferentially occupies the vacant Li sites in the trigonal LYC lattice, leading to the formation, growth, and eventual stabilization of an anode-electrolyte interphase (AEI) layer consisting of an In-doped $Li_{3-x}In_xYCl_6$ ($x = \approx 0.2$) phase. It is discussed how the presence of such an AEI layer prevents LYC decomposition and suppresses dendrite formation and propagation, enabling stable cycling of ASSB with ≈90% capacity retention over 1000 cycles. This work sheds light on the dynamic evolution of the halide SE and alloy anode interphase, and opens new avenues in the future design of long-lasting high-energy all-solid-state-batteries.

1. Introduction

Lithium-ion batteries (LIBs) with a liquid electrolyte have dominated the consumer electronics industries for decades.[1,2] Recent mass adoption in transportation electrification, however, has propelled the demands for safer and higher energy storage systems. Significant improvement in energy density, however, mandates the use of Li-metal anode which offers a high theoretical capacity (3860 mAh g^{-1}) along with the lowest negative potential. Yet the combination of a Li-metal anode with the carbonate-based liquid electrolytes in traditional LIBs has been proven problematic, as dendritic growth from the anode side leads to internal short-circuits and thermal runaway.[3,4] Non-flammable inorganic solid electrolytes (SEs), such as oxides and sulfides, are attractive alternatives. To that end, all-solid-state batteries (ASSBs) coupling an inorganic SE with a Li-metal anode are generally considered the future of energy storage technologies.[5–13]

A significant challenge facing the ASSBs is the electrochemical and chemical instabilities of the SEs at the Li-metal anode interface. For example, sulfide-based SEs (e.g., Li_3PS_4, Li_6PS_5X where X = Cl, Br, I, etc.) exhibit a high ion conductivity of > 1 mS cm^{-1} at room temperature (RT). Yet experimental results showed that upon direct contact with a Li-metal anode, the sulfides continuously decompose and produce a highly resistive anode electrolyte interphase (AEI) layer consisting of Li_2S, Li_3P, and PS_4^{3-} species, which eventually

S. Y. Kim, G. Chen
Energy Storage and Distributed Resources Division
Lawrence Berkeley National Laboratory
Berkeley, CA 94720, USA
E-mail: gchen@lbl.gov
S. Y. Kim
Energy Storage Research Center
Korea Institute of Science and Technology (KIST)
14 Gil 5 Hwarang-ro, Seongbuk-gu, Seoul 02792, Republic of Korea
S.-M. Bak
National Synchrotron Light Source II
Brookhaven National Laboratory
Upton, NY 11973, USA
S.-M. Bak
Department of Material Science and Engineering
Yonsei University
134 Shinchon-dong, Seodaemoon-gu, Seoul 03722, Republic of Korea
K. Jun, G. Ceder
Department of Materials Science and Engineering
University of California Berkeley
Berkeley, CA 94720, USA
K. Jun, G. Ceder
Materials Sciences Division
Lawrence Berkeley National Laboratory
Berkeley, CA 94720, USA

The ORCID identification number(s) for the author(s) of this article can be found under https://doi.org/10.1002/aenm.202401299

DOI: 10.1002/aenm.202401299

prevents ASSBs from cycling.[6,14–18] In addition, most sulfide SEs decompose at ≈2.7 V (Li^+/Li), limiting their use with a high-voltage cathode active material (CAM) such as $LiCoO_2$ (LCO) and $LiNi_xMn_yCo_{1-x-y}O_2$ (NMC).[12,13,19] One strategy in stabilizing the AEI layer in sulfide-based ASSBs is to employ a Li alloy anode instead of a Li-metal anode. Several lithium alloys such as Li-Si, Li-Mg, Li-In, and Li-Sn were investigated, and stable electrochemical cycling of sulfide ASSBs has been reported.[20–25] Especially, Li-In alloy anodes have been extensively used in laboratory ASSB studies as the alloying reactions occur at a stable redox potential of ≈0.62 V (vs Li^+/Li).[12] The alloys can be readily made by kneading a mixture of Li and In metals or by electrochemical reactions that form Li-In solid solutions with a specific ratio. To utilize the stable redox potential region, a two-phase system of (x)LiIn + (1-x) In ($0 < x \leq 1$) with low Li concentration is typically used.[26] Recent work by Zhang's group, however, showed that even with a Li-In alloy anode, Li_6PS_5Cl SE decomposes to In_2S_3 upon direct contact. The work further suggests that In_2S_3 can improve the wettability between Li-In and the SE, which facilitates Li-In dendrite growth along the SE grain boundaries and leads to eventual shorting and cell failure.[27]

In recent years, halide SEs (e.g., Li_3MCl_6, M = Sc, Zr, In, Y, Er, and Yb, etc.) have attracted much attention due to their superior oxidative stability and excellent chemical compatibility with uncoated 4 V-class CAMs.[28–32] Unfortunately, the halides also experience stability issues at the Li-metal anode. Experimental and theoretical studies showed that for Li_3YCl_6 (LYC) or Li_3InCl_6 (LIC) SEs, direct contact with Li-metal leads to halide decomposition. The result is the formation of an AEI consisting of poor Li conductors such as LiCl,[33] YCl_3, and/or $InCl_3$, along with metallic Y and/or In.[12,14,34,35] These processes largely limit the cycle life of halide-based ASSBs. As a mitigation approach, previous studies used Li_3PS_4 or Li_6PS_5Cl as a buffer layer between the halide SE and a Li-metal[28,31,36] or a Li-In alloy anode.[26] Recent reports, however, revealed chemical incompatibility between the halide and sulfide SEs which leads to decomposition reactions at their interface.[37] A few studies also investigated halide-based ASSBs without the presence of a buffer layer between the SE and the Li-In anode,[12,14,29,32,34,38,39] however, these investigations showed poor cycling performance. The interfacial chemistry at the anode remains largely unknown.

Herein, we constructed model halide ASSB cells with an LYC SE and a Li-In anode to investigate the chemical, structural, and morphological evolution at the anode interface. By incorporating a cracking-resistant single-crystal (SC) $LiNi_{0.8}Mn_{0.1}Co_{0.1}O_2$ (NMC811) as the CAM, we eliminate the uncontrolled impedance growth from contact loss between the CAM and SE that typically occurs in polycrystalline NMC811 based composite cathodes.[32,40–43] Through a combination of electrochemical and post-mortem analyses, we demonstrate the in situ formation and the dynamic evolution of an AEI layer during the ASSB cycling of over 1000 cycles. The chemical and structural nature of the AEI layer were elucidated through the high-resolution micro X-ray absorption spectroscopy (XAS) and X-ray diffraction (XRD) studies of the cycled ASSB pellets. Using density function theory (DFT) calculations, we reveal the mechanism of In^{3+} formation and subsequent migration into the vacant Li^+ sites in the LYC crystal structure during charge and discharge. Our findings provide new insights for designing functional AEI layers that enable the direct use of halide SEs with a Li-based anode in high-energy-density ASSBs.

2. Results and Discussion

2.1. Electrochemical Evaluation

We first evaluate the stability of LYC against a Li-metal anode and a Li-In alloy anode by comparing the overpotential evolution during the galvanostatic cycling of symmetric cells at a constant current density. At 0.2 mA cm^{-2}, the Li symmetric cell shows a gradual overpotential increase to ≈170 mV during the first 24 h (12 cycles) followed by a gradual decrease to ≈2 mV after ≈70 h (**Figure 1a**). The image obtained from the horizontally cross-sectioned Li symmetric cell after 50 h shows black deposits on the entire pellet surface (Figure S1a, Supporting Information). X-ray diffraction (XRD) analysis (Figure S1b, Supporting Information) shows LiCl as the main component of the deposits which is consistent with the previous reports.[12,14,34] It is possible that small amounts of other compounds (such as Y metal and/or YCl_3) are also present but were undetected by XRD.[14] Metallic Y is known to be highly reactive. It is possible that it reacted with the trace amounts of oxygen or carbon dioxide inside the glovebox, producing Y_2O_3 and/or $Y_2(CO_3)_2$. On the other hand, the Li-In alloy symmetric cell exhibits an initial overpotential of ≈150 mV before the gradual decrease during the subsequent 100 h cycling (50 cycles). The voltage reaches ≈60 mV and remains nearly constant through the rest of testing. In contrast to the Li symmetric cell, no discernible XRD peak shifts were observed and no new peaks were detected on the LYC SE layer recovered from the Li-In symmetric cell after cycling (Figure S1b, Supporting Information). The electrochemical impedance spectroscopy (EIS) data collected from the Li and Li-In symmetric cells further reveal the charge transfer behavior at the anode electrolyte interfaces. As shown by the semicircle on the Nyquist plot (Figure 1b), the initial charge transfer resistance (R_{ct}) in the Li cell is ≈49 Ω. After 50 h cycling, the semicircle effectively disappears, suggesting short-circuiting in the cell. On the other hand, while the Li-In cell shows a relatively large R_{ct} of ≈1260 Ω prior to cycling, it gradually decreases to ≈235 Ω after 50 cycles and remains stable until the end of the test, suggesting improved interface upon cycling. We assume this is due to the in situ formation of a more conducting anode-electrolyte interphase (AEI).

To further evaluate the anode interface, ASSB full cells were constructed with a $LiNi_{0.8}Mn_{0.1}Co_{0.1}O_2$ (NMC811) cathode and a Li-In anode. Single-crystal (SC) NMC811 particles, which have been shown to eliminate intergranular cracking and minimize the contribution of impedance growth at the cathode side, were directly used as CAM without a coating.[32,42] Maintaining cathode stability allows us to have a better-controlled investigation of the anode interface evolution.[32,43] Specifically, the cells were fabricated with a composite cathode of SC-NMC811/LYC/carbon (weight ratio = 57:40.5:2.5), an LYC SE separator, and a Li-In (3:7 mole ratio) alloy anode, similar to what was described in a previous publication.[32] An initial discharge capacity of 145 mAh/g was obtained at 0.5 C (Figure 1c,d) which is similar to what was reported on the equivalent cell using a liquid electrolyte. Stable cycling was achieved with a capacity retention of ≈88% after 1000 cycles. These results suggest a working mechanism where

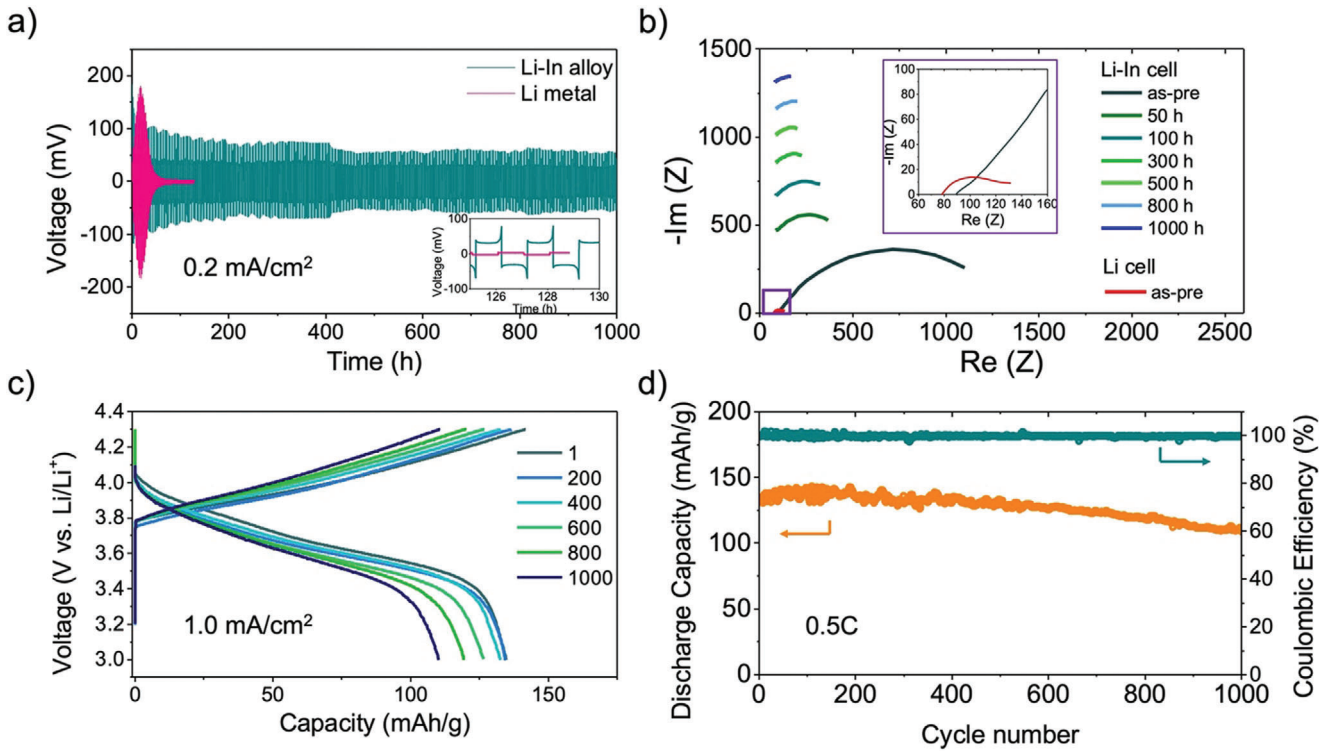

Figure 1. a) Cycling stability of Li|LYC|Li and Li-In|LYC|Li-In symmetric cells, b) Nyquist plots collected from the symmetric cells after various cycles. Inset: expanded view of the high-frequency region of the as-prepared symmetric cells. c,d) room-temperature charge/discharge voltage profiles and discharge capacity retention/coulombic efficiency of an SC-NMC811|LYC|Li-In ASSB cell cycled at 0.5 C, respectively.

stable charge transfer was established at the LYC SE and Li-In alloy interface and dendritic growth was suppressed even after prolonged cycling. To gain further understanding of the anode interface evolution, we carried out systematic analyses which are discussed in detail in the following sections.

2.2. Morphological Evolution and Chemical Analysis of the AEI Layer

The morphological evolution at the anode-electrolyte interface was investigated by post-mortem scanning electron microscope (SEM) imaging of the cross-sectional samples taken from the as-prepared ASSB pellet as well as recovered ASSB pellets after 50, 100, 500, and 1000 cycles, respectively. As shown in **Figure 2**a, the as-prepared interface shows a distinct boundary between the LYC and Li-In anode layers. After 50 cycles, a visible AEI layer with a thickness of ≈2–3 µm appears which grows to ≈5 µm after 100 cycles (Figure 2b,c). The layer thickness further increases to ≈50 µm after 500 cycles (Figure 2e, blue dotted lines outline the AEI region). Additional cycling to 1000 cycles appears to have little effect on the AEI thickness as it remains at ≈50 µm (Figure 2d). Some thickness variation across the interface is also observed, as shown in the low-magnification SEM images (Figure S2, Supporting Information) and Figure 2e. Distinct morphological contrasts among the layers of LYC, AEI, and the anode are clearly visible (Figure 2). Figure 2f–h shows the Energy Dispersive X-ray spectroscopy (EDX) maps of In *L*-edge, Y *L*-edge, and Cl *K*-edge collected from the sample after 500 cycles. It is evident that after cycling, In migrates into the AEI layer while Y remains in the LYC SE layer and the composite cathode only. As In is roughly 30% heavier than Y (atomic weight of 115 vs 89 g mol^{-1}), we believe that the presence of In in the AEI layer is largely responsible for the color contrast observed on the SEM images. We note that likely, the morphological changes between the layers also contributed to the observed contrast.

To further understand the nature of the AEI layer, we carried out a detailed chemical analysis at the anode interface. X-ray absorption near edge structure (XANES) spectroscopy was used to investigate the electronic structure of Y and In in the recovered cycled Li-In anode after 1000 cycles. The sample consists of the alloy anode along with the AEI component on the surface (schematics for the analysis shown in Figure S3a, Supporting Information). By comparing with the Y *K*-edge XANES spectra of Y^0 metal and Y^{3+} in as-prepared LYC SE (**Figure 3**a), we confirm that the oxidation state of Y in the cycled anode remains at 3+ (same as LYC). The changes observed in the lower *K*-edge intensity maxima (≈17.050 keV) and the suppressed peak evolution of multiple scattering in the post-edge region (> 17.050 keV) of the Y spectrum, however, suggest that the Y electronic structure is somewhat different from that in LYC. As the bulk-based XANES technique is known to be insensitive to small quantities of Y^0 that may result from LYC reduction,[14,34] we further used multi-energy micro hard X-ray absorption spectroscopy (µXAS) with a spatial resolution of 2 × 2 um^2 to perform Y chemical mapping on the recovered anode. The maps (Figure S4, Supporting

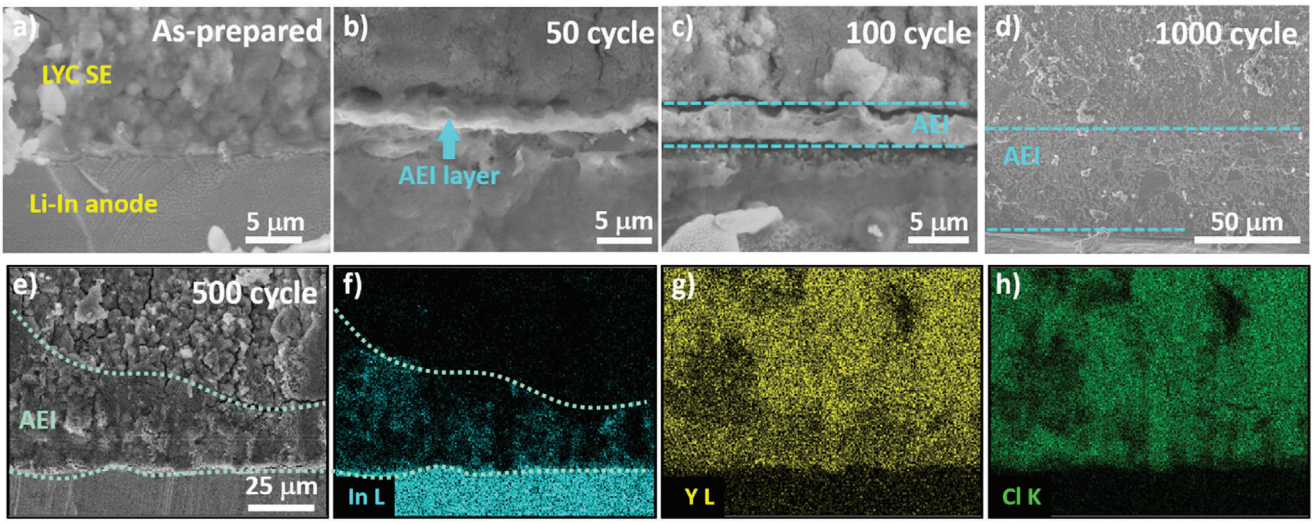

Figure 2. SEM images of the cross-sectioned ASSB pellets collected at the boundary between the LYC SE layer and the Li-In anode: a) as-prepared, b) after 50 cycles, c) after 100 cycles, and d) after 1000 cycles. e–h) SEM image and the corresponding EDX elemental maps of In, Y, and Cl were obtained on the ASSB pellet after 500 cycles. The dotted green lines outline the AEI regions.

Information) demonstrate a uniform areal distribution of the Y oxidation state, confirming the absence of locally reduced Y^0 and homogeneous Y^{3+} species in the AEI layer.

The XANES spectra of In *K*-edge collected on the cycled anode as well as those from various reference compounds are shown in Figure 3b. In the cycled anode, the In *K*-edge shifts from 27.936 keV to a higher energy of 27.937 keV ($\Delta = \approx 1$ eV), indicating the oxidation of In. As In in the bulk Li-In alloy anode is expected to remain in the metallic form, the results suggest that In in the AEI layer is oxidized. To better evaluate the chemical state of In, we employed X-ray fluorescence (XRF) elemental mapping and spatially-resolved Cl *K*-edge μXAS analysis in the cross-sectional area of ASSB pellets. The approach allows us to evaluate the chemical information of Cl in the AEI layer (in comparison to that in LYC), particularly changes in atomic coordination and symmetry around Cl anions revealed by the changes in the electron transition energy between Cl 1*s* and Y 4*d* – Cl 3*p* hybridized orbitals. The results obtained on the as-prepared ASSB pellet are shown in Figure S5 (Supporting Information). The cross-sectional XRF elemental map shows the initial distributions of Y, In, and Cl, represented in blue, green, and red colors respectively (Figure S5a, Supporting Information), confirming the distinct boundary between the LYC SE and Li-In anode without any elemental crossover between the layers. This is consistent with the results obtained from EDX analysis. Figure S5b (Supporting Information) compares the Cl *K*-edge μXAS spectra collected at two different locations (at a spot size of 5 × 5 μm^2) on the cross-section of the pellet: P1 in the LYC SE layer and P2 at the interface between Li-In and LYC SE. No differences are observed between P1 and P2 spectra, whose features are clearly distinguishable from those of the reference compounds (YCl_3, $InCl_3$, InCl, and LiCl) shown in Figure S5c (Supporting Information).

The XRF maps collected on the cross-section of the cycled ASSB pellet (Figure 3c–e), on the other hand, show In fluorescence signal in the LYC SE layer (red dotted box in Figure 3e right), indicating migration or diffusion into the LYC SE layer after cycling. We further collected Cl *K*-edge μXAS spectra at the various locations on the cross-section of the cycled ASSB pellet, marked as P1 in the composite cathode, P2 at the cathode-electrolyte interface, P3 and P4 in the LYC SE layer, P5 in the AEI layer and P6 in the alloy anode, respectively (Figure 3d). The collected μXAS data along with those from the reference compounds are displayed in Figure 3f,g. Compared to the reference spectra of LYC (P3), the similar profiles at the cathode and the cathode-electrolyte interface (P1 and P2) demonstrate the chemical stability of LYC against NMC811 under moderate ASSB cycling conditions, in accordance with the previous reports.[28,44] On the other hand, the Cl μXAS spectra collected near the AEI region (P4-P6) reveal changes in the covalency of Cl-metal bonds, evidenced by the electron transitions between Cl *1s* and Y 4*d* as well as the In 4*d* – Cl 3*p* hybridized orbitals. In contrast to the relatively weak and broad pre-edge peak at 28.233 keV (denoted as a) in LYC (P3), a prominent pre-edge peak at 28.245 keV (denoted as b) is clearly seen, especially at the AEI layer (P5). Further comparison with the spectra collected from the various metal (Li, Y, and In) chloride references reveals that the pre-edge peak maxima b strongly resembles that in $InCl_3$ (Figure 3g), indicating that the In 4*d* – Cl 3*p* orbital mixing in the AEI is similar to that of the In-Cl bonds forming the $InCl_6$ octahedra in $InCl_3$. It should be noted that a similar pre-edge feature of Cl octahedra was also observed on the In-doped LYC phases ($Li_3Y_{1-x}In_xCl_6$, $0.2 < x \leq 1$).[45,46] One can expect the presence of this feature in a similar In-doped LYC series of $Li_{3-x}In_xYCl_6$ ($x \leq 0.2$), although these compounds have not been synthesized or reported. The distinct Cl pre-edge feature in $InCl_3$ is due to an open shell electron structure (i.e., filled valence shell $d^{[10]}$) of In^{3+} that partially allows a forbidden $1s \rightarrow 3d$ transition when it is ligated to Cl^-, through the mixing of ligand *p*-orbitals with metal *d*-orbitals with a significant contribution of Cl 3*p* character.[47–49] For InCl with a closed shell In^{1+}, although the Cl *K*-edge peak maxima (labeled as c in Figure 3g) is close to peak b in the AEI layer, the differences

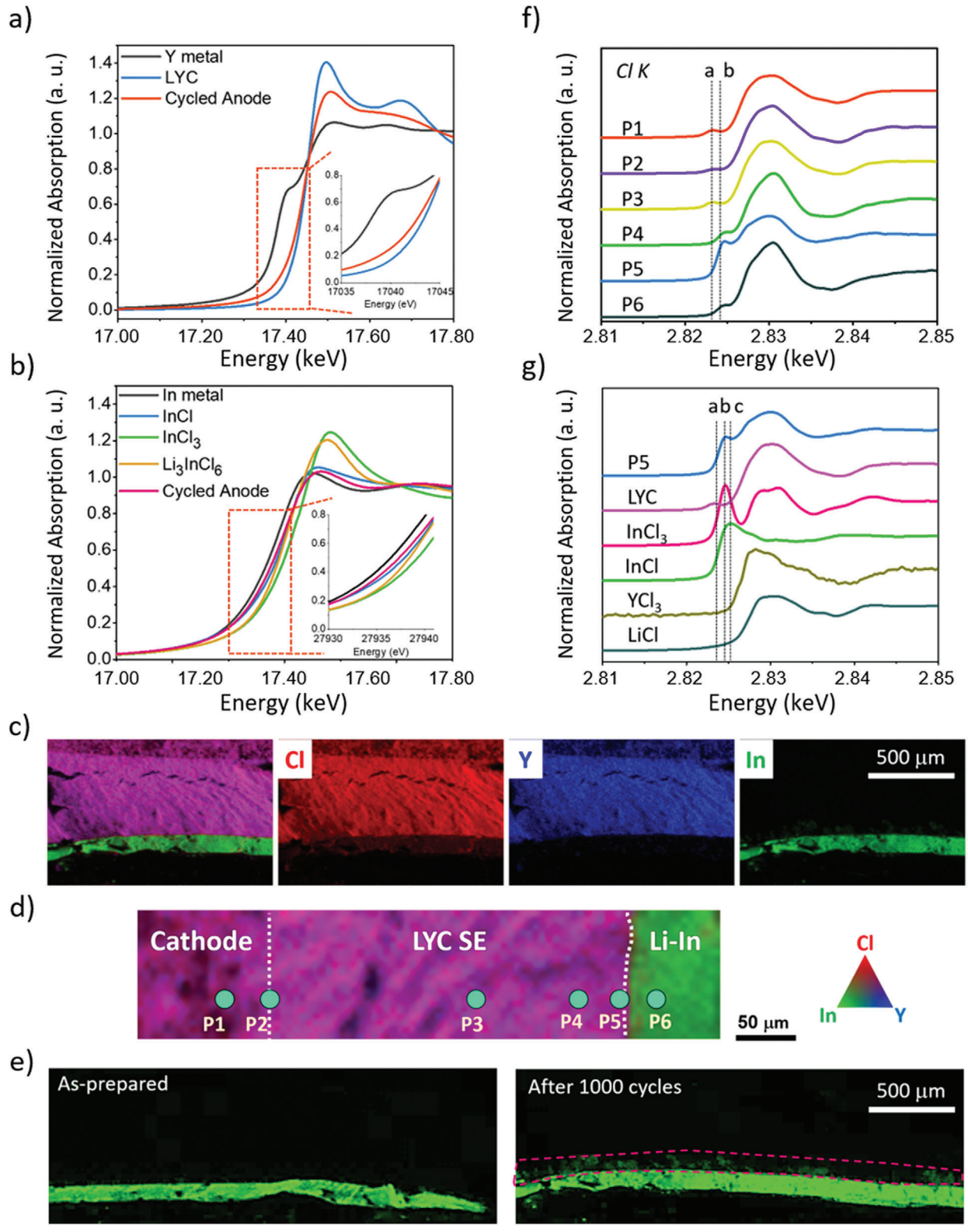

Figure 3. a,b) Y *K*-edge and In *K*-edge hard XAS spectra collected on the various samples as indicated, respectively. c) XRF elemental maps for Y, In, and Cl were collected on the cross-section of the ASSB cell after 1000 cycles. d) Expanded cross-sectional view of the XRF map collected on the cycled ASSB showing the boundaries between the SC-NMC811 composite cathode, LYC SE, and Li-In anode. The blue dots indicate the locations (P1-P6) where the Cl *K*-edge μXAS spectra were collected. e) Comparison of the In XRF maps before and after 1000 cycles. f) Cl *K*-edge uXAS spectra were collected at various locations as shown in Figure (d). g) Comparison of Cl *K*-edge uXAS spectra collected from the AEI layer (P5) and various reference compounds.

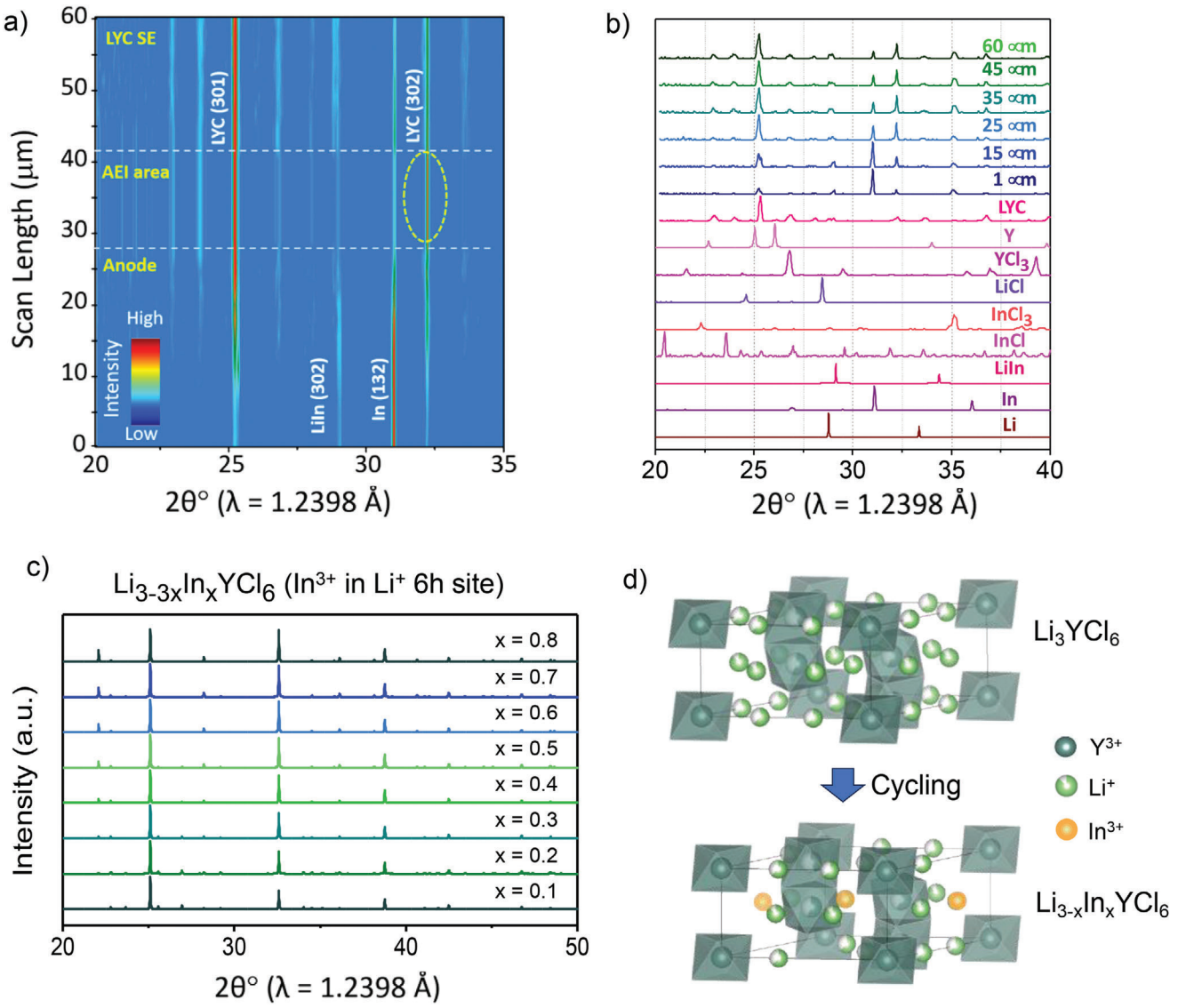

Figure 4. a) A color contour map of the μXRD patterns collected from the cross-section of the recovered ASSB pellet after 1000 cycles. The color scheme indicates XRD peak intensities. b) μXRD patterns collected at the various locations as indicated in Figure S3b (Supporting Information) as well as from various reference compounds. c) Simulated XRD patterns of $Li_{3-x}In_xYCl_6$ ($0.1 \leq x \leq 0.8$) where Li^+ 6 h sites are partially occupied by In^{3+}. d) Atomic arrangements in trigonal LYC and $Li_{3-x}In_xYCl_6$. The increase in LYC (302) XRD peak intensity in the 27–41 μm range is highlighted in the yellow dotted circle in (a) and the shaded rectangle in (b) and (c).

observed in the pre- and post-edge regions indicate a low probability of InCl in the AEI layer. The most likely components in the AEI layer, therefore, are indium-containing chlorides with the octahedral In-coordination environment, such as $InCl_3$ and In-doped $Li_3Y_{1-x}In_xCl_6$ or $Li_{3-x}In_xYCl_6$. As $InCl_3$ coating has been used to enhance the charge transfer from the electrode surface[50] and In-doped $Li_3Y_{1-x}In_xCl_6$ showed better ionic conductivity than LYC,[45] their presence at the interface is likely to improve ASSB performance, especially during their formation in the early cycles. This is consistent with our results from electrochemical evaluation (Figure 1a,b). We note the results from combined XRF elemental mapping and Cl *K*-edge μXAS analysis do not exclude the possible presence of metal chlorides due to LYC decomposition, including YCl_3 and LiCl.

2.3. Structural Analysis of the AEI Layer

The structural evolution of the AEI layer was further investigated using the micro X-ray diffraction (μXRD) technique. The sampling procedure and sample mounting configuration for the measurement are shown in Figure S3a,b (Supporting Information), respectively. The patterns were collected on the cross-sectional area of the as-prepared and cycled ASSB pellets. **Figure** 4a shows the color contour plot of the collected patterns where the peak intensity is indicated by the color scheme in the map (red for high intensity and blue for low intensity). The μXRD scans from the starting point to 15 μm are dominated by reflections from the Li-In alloy (Figure 4b). As the alloy exists as a solid solution of metallic In and the intermetallic Li-In phase (7In + 3LiIn for a target

composition of Li: In = 0.3: 1), the strong (132) peak from In at $2\theta = \approx 31°$ dominates the μXRD pattern. The weak (302) peak of Li-In is also observed through the reflections from the <022> plane at $2\theta = \approx 29.3°$ and the <113> plane at $2\theta = \approx 34.3°$.[20,26] Increasing Li content in Li_xIn (up to $x = 0.7$) maintains the same crystal structure of the phase, however, the <113> peak intensity decreases.[51] A weak signal of the LYC (301) peak was also observed due to the X-ray scattering from the LYC debris near the Li-In anode. Starting at around 25 μm, this peak becomes much more intense while the peaks of Li-In and In diminish, indicating that the μXRD scanning reaches the AEI layer close to the LYC SE. From the subsequent scans up to around 41 μm, the μXRD patterns show a distinctive intensity increase of the LYC (302) peak (at ≈32.4°) in the AEI layer (highlighted in orange color in Figure 4b), as compared to the pristine LYC. Note that the Bragg reflection peaks of LYC are indexed based on the structure model of the mechanochemically synthesized LYC phase (Table S1, Supporting Information).[29,52]

The comparison with the reference XRD patterns confirms the absence of LYC decomposition products (Y metal, LiCl, and YCl3). We hypothesize that the intensity increase at ≈32.4° is due to form factor changes of the LYC (302) plane. To investigate, we studied the following scenarios where an increase in (302) reflection intensity in LYC is possible: 1) modified Y^{3+} occupancy in Li^+ and Y^{3+} sites due to Y migration and 2) introducing In^{3+} into Li^+ or Y^{3+} sites during cycling of the ASSB cell. The corresponding XRD patterns of the modified LYC in each scenario were simulated, and the intensity changes in (302) reflection were compared. Among various trigonal LYC crystal models, the XRD peak intensity at ≈32.5° only increases when In^{3+} occupies Li 6 g or 6 h sites of trigonal LYC, as shown in Figure 4c-d and Figure S6 (Supporting Information). This suggests that in our electrochemical cycling, In^{3+} migrates into the 6 g or 6 h Li^+ sites (V'_{Li}) in the LYC lattice while Li^+ moves out of these sites without Cl^- sublattice rearrangement, leading to the formation of trigonal $Li_{3-3x}In_xYCl_6$ phase. Based on the peak intensity ratio, the x value is estimated to be ≈0.2, which is the In solubility limit in the $Li_{3-3x}In_xYCl_6$ phase.

Thermodynamically, In prefers to occupy the Y sites in the LYC structure which leads to the structural change from the trigonal Li_3YCl_6 to monoclinic $Li_3Y_{1-x}In_xCl_6$ ($x > 0.2$).[45] This was evident in our failed attempt to experimentally obtain the $Li_{3-3x}In_xYCl_6$ phase. During the synthesis, the ball-milling method was used on various powder precursors, including a series of LiCl, (1-x)YCl_3, and xInCl mixtures and (3-3x)LiCl, YCl_3, and $x$$InCl_3$ mixtures. Here x indicates the mole ratio of the InCl precursor used in the synthesis. In all cases where $x < 0.5$, we obtained the final products with the In^{3+} occupying the V'''_Y site instead of the V'_{Li} site, leading to the formation of the $Li_3Y_{1-x}In_xCl_6$ phase (Figure S7, Supporting Information). Despite the fact that the ionic radius of In^{3+} to Li^+ are closer in value (Li^+: 0.76Å, In^{3+}: 0.8Å, and Y^{3+}: 0.9Å), our experimental effort to synthesize the metastable $Li_{3-3x}In_xYCl_6$ compounds was unsuccessful.

Under kinetic conditions, however, the occupancy of V'_{Li} site by metal cations in SEs is plausible. Wagemaker et al. recently reported the delithiation of solid electrolytes, such as Li_6PS_5Cl, during electrochemical cycling.[53] The design and synthesis of Al-argyrodite $(Li_{5.7}Al_{0.1})PS_5I$ utilize the substitution of Al into the Li site of Li_6PS_5I, which demonstrates the feasibility of cation mixing between Li and metal cations in SEs.[54] We speculate that during electrochemical cycling, the movement of Li^+ provides a kinetic driving force for In^{3+} migration into the in situ generated V'_{Li} sites, leading to its preferred occupancy in the V'_{Li} site instead of the V'''_Y site of the LYC lattice. Traditionally, the feasibility of ion migration into the SE crystal lattice has been evaluated by measuring bulk AC impedance or by computing theoretical ion migration activation energies within the lattice.[55–58] However, as the AC impedance evaluates the total cation migration resistance from the SE, it is difficult to deconvolute and determine only the In^{3+} migration impedance in the AEI layer. To this end, we adopted theory studies to further understand the mechanism of In^{3+} migration in LYC and the chemical evolution of the AEI layer.

2.4. Mechanistic Understanding by DFT Calculations

Nudged elastic band (NEB) calculations based on density functional theory were performed to evaluate the In^{3+} migration energy within the hexagonal close-packed Cl^- sublattice of LYC. As shown in **Figure 5**, In^{3+} migration along the in-plane and out-of-plane channels in the LYC anion sublattice requires a migration energy of 0.873 eV and 0.913 eV respectively. We note that this value only captures the interaction between the In^{3+} and Cl^- sublattice without considering any interactions between cations. However, our result provides a reasonable approximation of the actual In^{3+} migration energy in LYC as the high polarizability of the Cl^- sublattice likely screens out most of the interactions between cations. NEB calculations indicate that In^{3+} migrates through an intermediate tetrahedral site (Oct-Tet-Oct) for both the in-plane and out-of-plane channels. When compared to the migration energy of multivalent cations in oxide systems, the calculated In^{3+} migration energy is low enough to allow gradual In^{3+} migration into the LYC lattice during long-term electrochemical cycling.[59–62]

To understand the thermodynamic driving force (ΔG)for the insertion of In^{3+} and extraction of 3 Li^+ upon discharging to form $Li_{3-3x}In_xYCl_6$, we calculated the energy of various enumerations of ion configurations in LYC where 3 Li^+ are replaced by 1 In^{3+} ($3Li^+ \rightarrow In^{3+}$). During discharge, the driving force for this reaction is −12.98 eV (see Experimental Section). Thus, within the operating condition of using LYC as the solid electrolyte against the Li-In anode, there is a strong driving force to spontaneously form $Li_{3-3x}In_xYCl_6$. In addition, to understand the thermodynamic stability of $Li_{3-3x}In_xYCl_6$, we computed the energy above the convex hull of the lowest energy enumeration of $Li_{3-3x}In_xYCl_6$ ($x = 1/6$) to be 0.028 eV per atom, which is only slightly higher than the lowest energy enumeration of pristine LYC (0.022 eV per atom). Therefore, the incorporation of In^{3+} in the Li-site of LYC does not destabilize the LYC structure significantly. When comparing In^{3+} occupying the 6 g Li site and the 6 h Li site, we found that In^{3+} prefers to occupy the latter ($E_d = 0.304$ eV per defect) rather than the former ($E_d = 0.527$ eV per defect) (Figure S8, Supporting Information). This is possibly due to the lower occupancy of Y^{3+} near the Li 6 h sites which leads to less electrostatic repulsion for In^{3+}. The results from the DFT calculations further confirm that In^{3+} cations preferentially migrate into the trigonal LYC framework especially into Li^+ 6 h sites, leading to the formation

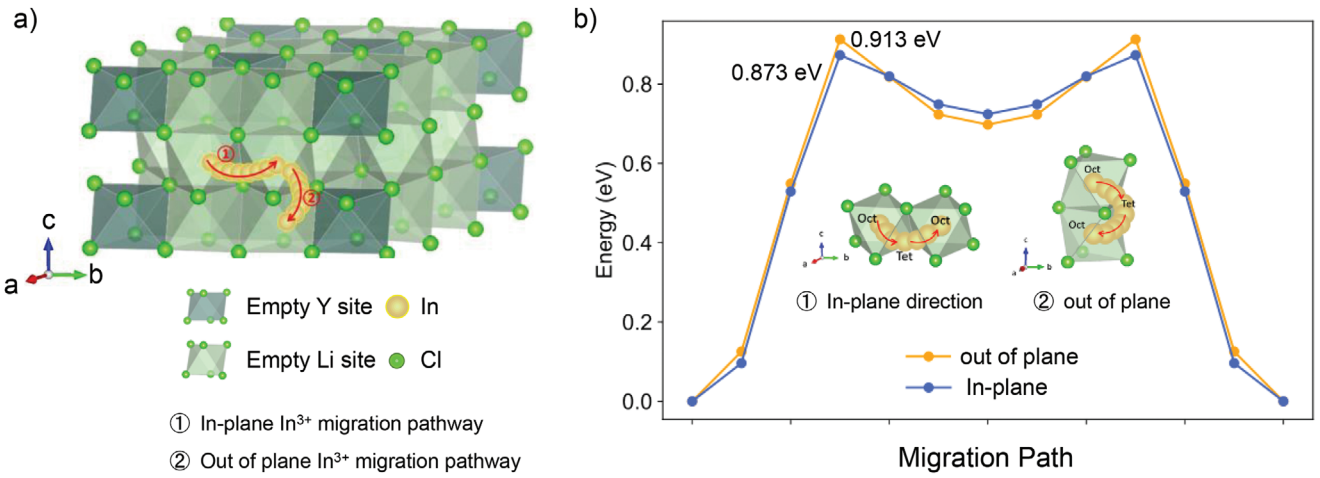

Figure 5. a) Visualization of predicted In^{3+} ion migration pathways in trigonal $Li_{3-3x}In_xYCl_6$ crystal structure. The anion sublattice of trigonal LYC without any cation is employed to calculate the In^{3+} ion migration energy. b) Calculated In^{3+} ion migration energy barrier along the predicted 1) in-plane and 2) out-of-plane In^{3+} ion migration pathways (inset).

of $Li_{3-3x}In_xYCl_6$ through a dynamic doping process during electrochemical cycling.

Based on the calculated positive reaction energy between LYC and In (Table S2, Supporting Information), we believe that a spontaneous chemical reaction between LYC and Li-In is unlikely. This was further supported by the negligible morphological changes between LYC and Li-In anode after 30 days of physical contact (Figure S9a,c, Supporting Information), as compared to the clear morphological changes after cycling (Figure S9b,d, Supporting Information).

2.5. Discussion

The combined experimental and theoretical results show that instead of LYC reducing to YCl_3, LiCl, and Y metal, an AEI layer of $Li_{3-3x}In_xYCl_6$ forms. The value of x and the thickness of the AEI layer increase during the early cycles and stabilize after extended cycling, reaching ≈0.2 and 50 µm after 1000 cycles, respectively. Based on these observations, we propose a mechanism for AEI evolution and discuss its effect on dendrite formation and propagation.

The schematics of the ASSB cells consisting of an NMC811 composite cathode, an LYC separator, and a Li-In alloy anode are shown in **Figure 6**a. In a scenario where dendrites of Li or Li-In nucleate at the anode interface, they can react with LYC and lead to its decomposition to YCl_3, LiCl, and Y metal. This may occur either due to local anode potential variations or slow diffusion of Li^+ into the alloy anode, both of which can cause a voltage drop below that of LYC reduction (0.62 V). The dendrites then continue to grow and after extended cycling, form an internal short through the SE layer (Figure 6b, *dendrite growth model*). This is similar to what was previously reported on the sulfide SE-based ASSB cells.[27,63] On the other hand, the formation of $Li_{3-3x}In_xYCl_6$ and its dynamic evolution in the AEI layer largely prevent such a process. As shown in Figure 6c (*dynamic AEI evolution model*), upon the 1st charge, Li^+ moves from the NMC811 cathode to the Li-In anode, gets reduced, and is incorporated into the Li-In alloy or forms dendrites. During the 1st discharge, Li^+ gets generated at the anode and moves toward the cathode to be intercalated into NMC811. During the process, Li^+ also moves from LYC SE to the NMC811 cathode and leaves vacancies behind. In in the Li-In anode gets oxidized to In^{3+} and migrates into the vacant Li sites in the LYC lattice. During the 2nd charge, Li^+ moves from the cathode to the anode for the reduction reaction. We believe that some Li^+ also moves into the LYC lattice to replace In^{3+} in the Li site. This is because the x value and the thickness of the $Li_{3-3x}In_xYCl_6$ AEI layer stabilize after ≈500 cycles. Afterward, the cell continues to cycle with no net increase in them, reaching steady states. This suggests that In^{3+} migration occurs in both ways. The replaced In^{3+} then moves toward the anode and gets reduced (Figure 6c, highlighted in the pink rectangle). The migrating Li^+ and In^{3+} cations may also nucleate into Li-In at the surface of the anode where the high electronic conductivity provides a lithiophilic environment (Figure 6c, highlighted in the green rectangle). The following discharge repeats the same processes as in the 1st discharge.

These individual processes likely compete with each other and the varied dynamics continue until reaching the In solubility limit in the trigonal $Li_{3-3x}In_xYCl_6$ phase ($x = \approx 0.2$). Before reaching the In solubility limit in the $Li_{3-3x}In_xYCl_6$ phase, one can expect a net effect of more In^{3+} migrating into the LYC lattice, and the x value increases. Once reaching the limit, there are no net changes in x value and the dynamic processes reach a steady state. The net effect of charge and discharge then becomes Li^+ migrating between the cathode and anode (same as the typical lithium-ion batteries), albeit with accompanying In redox reactions and In^{3+} movement. In a given cell configuration, the thickness of the $Li_{3-3x}In_xYCl_6$ AEI layer is likely determined by the amount of Li^+ moved between the cathode and anode, or the current density used during the cycling.

The proposed dynamic AEI evolution model is also supported by the decreasing AEI resistance during the initial cycling (Figure 1). For each In^{3+} replacing 3 Li^+, two V'_{Li} sites are generated. This lowers the Li migration energy and improves the ionic conductivity, similar to the scenario where aliovalent cation

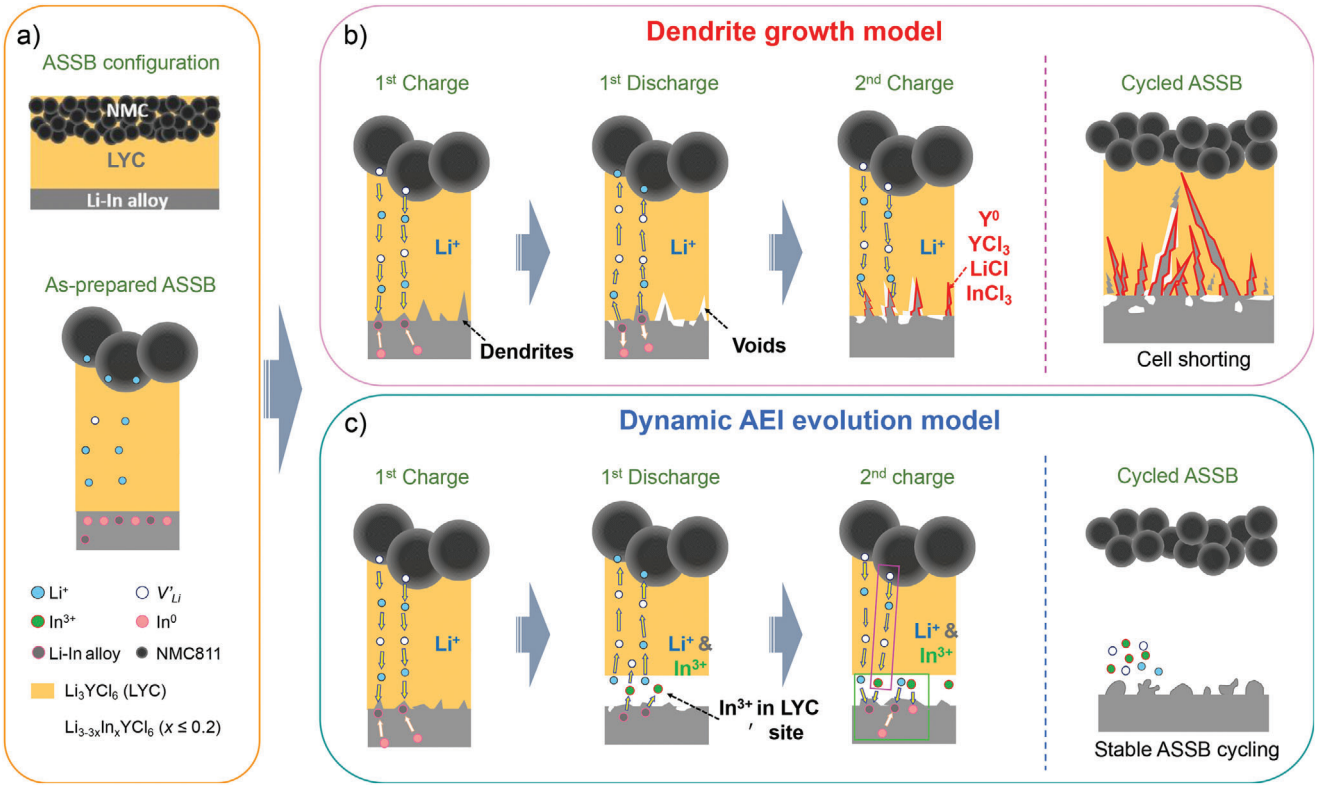

Figure 6. Schematics of the proposed models for LYC and Li-In anode interface evolution upon cycling: a) As-prepared ASSB configuration and Li^+, In^{3+} and V'_{Li} sites in the corresponding cell components, b) LYC decomposition accompanied by Li-In dendrite growth model, and c) the formation and evolution of an AEI layer with the dynamic movement of In^{3+} and Li^+ cations in and out of the LYC structure in the AEI layer. Dendrite growth is suppressed in this model.

doping in SEs enhances the ionic conductivity.[30,31] The correlation between the amount of In^{3+} occupying the Li 6 h site in LYC and Li^+ migration kinetics during the ASSB cycling, however, is unclear at this time and it requires further investigation. For the future design of high-energy ASSBs, it is crucial that the alloy anodes have a solid-solution phase with high Li solubility, appropriate redox potentials (above the halide SE reduction potential while minimizing the energy loss due to the elevated anode potential), chemical and electrochemical stabilities.

3. Conclusion

In this study, we developed and evaluated cell designs for halide-based ASSBs without the use of a buffer layer between the SE and a Li-metal-based anode. Excellent cycling stability was achieved on cells consisting of a composite cathode of uncoated SC-NMC811/LYC/carbon, a LYC SE, and an Li-In alloy anode, delivering a discharge capacity of 145 mAh g^{-1} at 0.5 C and a capacity retention of ≈90% after 1000 cycles. We revealed that along with the migration of Li^+ during discharge and charge, In in the alloy anode gets oxidized and reduced, respectively. The in situ formed In^{3+} migrates into the vacant Li sites in the trigonal LYC lattice and the dynamic processes lead to the formation of an AEI composed of a trigonal $Li_{3-x}In_xYCl_6$ phase. Both the x value and the thickness of the AEI layer stabilize over cycling, reaching a steady state. The unique evolution of the AEI layer enables stable cell cycling of the ASSB cell by preventing LYC decomposition and suppressing dendrite formation. We believe the findings from this study, particularly the migration of In^{3+} from the anode into the Li site in LYC and the consequent transformation of LYC into a $Li_{3-x}In_xYCl_6$ AEI layer, open up a new avenue in designing stable anode-electrolyte interfaces for high-energy all-solid-state batteries.

4. Experimental Section

Materials Synthesis: Li_3YCl_6 solid electrolyte powder was prepared by the ball milling synthesis method as previously described.[32] Stoichiometric mixtures of LiCl (Thermo Scientific Chemicals, ultra-dry, 99.995%) and YCl_3 (Sigma-Aldrich, 99.9%) were ground together in an agate mortar inside an Ar-filled glovebox. The mixture was then placed into a ZrO_2 jar with ZrO_2 balls (diameter = 10 mm) which was sealed inside the glovebox prior to the ball milling. High-energy ball milling was carried out at 550 rpm for 48 h at room temperature, using a planetary ball mill from Retsch (PM200). Single-crystal $LiNi_{0.8}Mn_{0.1}Co_{0.1}O_2$ (SC-NMC811) were obtained from a commercial source. Indium (Sigma-Aldrich, 99.99%) and lithium (Thermo-scientific, 99.9%) metal disks were used as received to prepare Li-In alloy anodes, as described in our previous publication.[32]

Characterization: Powder X-ray diffraction analysis was conducted by using a Bruker D2 Phaser powder X-ray diffractometer equipped with the Cu-Kα (λ = 1.54 Å) radiation. All SEM images and the corresponding elemental mapping by EDS were carried out using a JEOL JSM-7500F field emission scanning electron microscope at an accelerating voltage of 15 kV.

To prepare the cross-sectional samples of the recovered ASSB pellets, the cycled pellet was carefully removed from the pellet-die-shaped cell cage inside of an Ar-filled glove box. The retrieved pellet was then cut into small pieces using a surgical knife blade to make sharp and clean edges of the ASSB cross sections.

Hard XAS measurements for Y and In *K*-edges were performed at Stanford Synchrotron Radiation Lightsource (SSRL) beamline 2-2. Prior to the measurements, a small piece was carefully cut out of the ASSB pellet using a sharp knife. Li-In anode was detached from the piece by removing the layers of cathode and LYC SE. The LYC that remained on the top of the recovered Li-In anode was carefully removed by using a stainless-steel brush and sandpaper (the procedure is shown in Figure S3a, Supporting Information). All samples were sandwiched in Kapton films for the measurements with a Si(220) crystal applied as a monochromator. Monochromatic energy calibration was accomplished by the E_0 value of 17.038 keV and 27.940 keV for Y and In metal foil references, respectively. The collected XANES data was processed by Sam's Interface for XAS Package (SIXPACK) software.[64]

Multiple-energy μXAS chemical analysis of Y was carried out at SSRL beamline 2–3. For μXANES mapping, energy calibration was achieved by using the center of the pre-edge of Yttrium metal at 17.038 keV. Electrode samples sandwiched between Kapton tapes were placed 45° to the incident X-ray beam. Multiple Y *K*-edge data were collected by exciting ten incident X-ray energies near Y *K*-edge in an energy range centered at 17.050 keV, within an energy window of 100 eV. The Y chemical maps were collected on the recovered Li-In anode surface within an area of 1×2 mm^2 which was in direct contact with LYC SE. The data collection started from a 2×2 μm^2 area and then moved to a 2 μm per dataset within the sampled area. Each dataset consists of averaged three scans with a data collecting step size of 2 μm and a beam exposure time of 25 ms per step. The collected data was processed using Sam's Microprobe Analysis Kit (SMAK) software.[65]

X-ray fluorescence (XRF) imaging and Cl *K*-edge μXAS analysis was carried out at the beamline 8-BM (TES) of the National Synchrotron Light Source II (NSLS-II) at Brookhaven National Laboratory (BNL). ASSB pellet sample was cross-sectioned using a sharp surgical knife and mounted onto a sample holder specifically designed for cross-sectional imaging at TES. The samples were fixed in the position using a Cu tape and then covered with a Mylar film to avoid air exposure. The XRF/μXAS measurement was conducted in the He-filled chamber at the TES beamline to minimize air exposure. XRF imaging was performed in a fly scan mode with a 5 μm pixel size. The X-ray energy was set at 2900 eV to obtain the elemental map of Cl, Y, and In. After XRF imaging, the μXAS was collected at selected spots using the same size of micro-beam, 5 μm (horizontal) × 5 μm (vertical). XANES data were analyzed using the Demeter software package.[73]

Synchrotron μXRD measurements were performed at beamline 12.3.2 at the Advanced Light Source (ALS) at Lawrence Berkeley National Laboratory (LBNL).[66] The μXRD sample was prepared inside of an Ar-filled glove box. ASSB pellet sample was carefully cut into a rectangular shape using a sharp surgical knife, vertically mounted onto a glass slide, and fixed in position using carbon tape. The sample holder was then covered by a Teflon tape to prevent the sample from possible air exposure during the μXRD data collection (Figure S3b, Supporting Information). The μXRD data was collected by moving the sample stage at a 2 μm $^{-1}$scan rate for a total of 30 scans, using linear μXRD scan between the Li-In anode and LYC SE near the AEI layer. For the measurement, a 10 keV ($\lambda = 1.2398$ Å) monochromatic X-ray beam was focused to ≈2×2 μm^2 by Kirkpatrick-Baez mirrors.

Cell Fabrication and Electrochemical Evaluation: The electrochemical evaluation was performed in homemade cells consisting of a zirconia ceramic mold (inner diameter is 0.5 inch) cell body and two stainless-steel rods as current collectors.[32] For symmetric cells, the synthesized LYC powder was first pelletized at 300 Mpa inside an Ar-filled glove box. Li-In alloy anode was prepared by kneading the Li and In metals together, with a target molar ratio of Li:In = 3:7. Alloy disks with a diameter of 0.5 inch and a thickness of ≈250 μm were then punched out. The prepared anodes were then placed on both sides of the LYC pellet. The assembled symmetric cell was then placed into a pressure jig and cycled at a current density of 0.2 mA cm^{-2} under a constant pressure of ≈8 Mpa. The EIS measurements were conducted within the frequency range of 1–10 mHz using a constant voltage of 10 mV. To assemble the ASSB cells, a mixture of SC-NMC811, LYC, and carbon black (Denka black) powder was mixed in a weight ratio of 60:38:2 and ground for 20 min by hand grinding. The composite cathode was then spread onto the pelletized LYC SE layer. The two components were then pressed firmly together under 300 Mpa applied pressure to secure the contact between the composite cathode and the SE layer. The prepared Li-In disk was then placed onto the LYC pellet to serve as the anode, following the procedure previously reported in the literature.[32] The assembled ASSB cells were placed into a pressure jig and galvanostatically cycled 0.5C (1C = 200 mAh g^{-1}) in a voltage window of 3–4.3 V (vs Li$^+$/Li), under an external pressure of ≈8 Mpa. All electrochemical testing was carried out inside an Ar-filled glove box at ambient temperature, using a VMP3 (Bio-Logic) cycler.

DFT Calculations: The driving force to form $Li_{3-3x}In_xYCl_6$ during discharge (ΔG) was calculated using the following equation:

$$\begin{aligned}\Delta G &= E_{doped} - E_{pristine} + \sum_i \Delta n_i \mu_i = \left(E_{doped} - E_{pristine}\right) - \mu_{In}^{anode} \\ &+ 3\mu_{Li}^{cathode} + 3\left(\eta_e^{cathode} - \eta_e^{anode}\right) = \left(E_{doped} - E_{pristine}\right) - \mu_{In}^{anode} \\ &+ 3\mu_{Li}^{cathode} - 3e \times OCV \end{aligned} \quad (1)$$

where E_{doped}, $E_{pristine}$, Δn_i, μ_i, η_e are the bulk energy of the doped structure with In insertion and 3 Li removal, the bulk energy of the pristine Li_3YCl_6 structure, the number of atoms of element *i* that are being added or removed, the chemical potential of element *i*, and the electrochemical potential of the electron. Since an electron is carried from the anode to the cathode in this reaction, the electron electrochemical potential (η) in the cathode and anode must be included. As LYC is interfacing with the Li-In anode during discharge, the In chemical potential within the Li-In anode of −0.01 eV versus In-metal and the Li chemical potential within the cathode of −3.8 eV versus Li-metal for NMC-811 was taken. An experimental open circuit voltage of 2.82 V was used. Li/vacancy and Y/vacancy were enumerated orderings in the disordered Li_3YCl_6 structures reported from previous mechanochemical synthesis.[67] Enumerations were performed using Pymatgen[68] on ($1 \times 1 \times 2$) supercell, and 25 distinct structures with the lowest Ewald electrostatic energy were selected for DFT calculations. Using the lowest energy enumerated LYC structure, three Li$^+$ with one In^{3+}, and 30 distinct structures were substituted with the lowest Ewald electrostatic energies selected for DFT calculations. To compute the energy above the convex hull, Pymatgen[68] was used to build the convex hull of Li-In-Y-Cl space after combining all Materials Project entries within this chemical space with our DFT enumerations. For calculating the migration energy of In^{3+}, a ($1 \times 1 \times 2$) supercell was used for the reported LYC crystal structure with cation site disorder induced by mechanochemical synthesis method for nudged elastic band (NEB) calculations.[67] In^{3+} was inserted into the octahedral site of the hcp Cl$^-$ sublattice. Background charges were applied to maintain the valence of Cl$^-$ and In^{3+}. NEB calculations were converged with force criteria of 0.01 eV Å^{-1}. The position of every atom was allowed to be optimized during the NEB calculation.

All DFT calculations were performed using the Vienna ab initio simulation package (VASP)[69] within the projector augmented wave formalism.[70] The generalized gradient approximation (GGA) exchange-correlation functional[71] was used with an energy cutoff of 520 eV. K-point grids that are compatible with the Materials Project database were used.[72] All structures were converged to 10^{-5} eV in energy and 0.01 eV Å^{-1} in the forces.

Supporting Information

Supporting Information is available from the Wiley Online Library or from the author.

Acknowledgements

The authors thank Drs. Erik Nelson, Matthew Latimer, and Leah Kelly for helping with the hard XAS measurements, and Drs. Sam Webb and Sharon Bone for helping with micro-XAS measurements and data analysis at SSRL. Use of SSRL, SLAC National Accelerator Laboratory was supported by the U.S. Department of Energy, Office of Science, Office of Basic Energy Sciences under Contract No. DE-AC02-76SF00515. The authors also thank Dr. Nobumichi Tamura at the ALS for helping with the μXRD measurements and discussions. ALS at LBNL was a DOE User Facility under Contract No. DE-AC02-05CH11231. This research used beamline 8-BM (TES) of the National Synchrotron Light Source II, U.S. DOE Office of Science User Facilities operated for the DOE Office of Science by Brookhaven National Laboratory under Contract No. DE-SC0012704. Prof. S.-M.B. acknowledges support from the Yonsei University Research Fund (2023-22-0158). S.Y.K. acknowledges support from the Korea Institute of Science and Technology (KIST) Institutional Program (Project no. 2E32581). This work was supported by the Assistant Secretary for Energy Efficiency and Renewable Energy, Office of Vehicle Technologies, of the U.S. Department of Energy under Contract No. DE-AC02-05CH11231.

Conflict of Interest

The authors declare no conflict of interest.

Data Availability Statement

The data that support the findings of this study are available from the corresponding author upon reasonable request.

Keywords

all-solid-state batteries, anode-electrolyte interface, halide solid electrolyte, Li-In anode, NMC cathode

Received: March 21, 2024
Revised: April 15, 2024
Published online:

[1] L. Trahey, F. R. Brushett, N. P. Balsara, G. Ceder, L. Cheng, Y.-M. Chiang, N. T. Hahn, B. J. Ingram, S. D. Minteer, J. S. Moore, K. T. Mueller, L. F. Nazar, K. A. Persson, D. J. Siegel, K. Xu, K. R. Zavadil, V. Srinivasan, G. W. Crabtree, *Proc. Natl. Acad. Sci. USA* **2020**, *117*, 12550.
[2] M. Armand, J.-M. Tarascon, *Nature* **2008**, *451*, 652.
[3] K. Liu, Y. Liu, D. Lin, A. Pei, Y. Cui, *Sci. adv.* **2018**, *4*, eaas9820.
[4] L. Bravo Diaz, X. He, Z. Hu, F. Restuccia, M. Marinescu, J. V. Barreras, Y. Patel, G. Offer, G. Rein, *J. Electrochem. Soc.* **2020**, *167*, 090559.
[5] J. Wolfenstine, J. Allen, J. Read, J. Sakamoto, *J. Mater. Sci.* **2013**, *48*, 5846.
[6] S. Wenzel, S. Randau, T. Leichtweiß, D. A. Weber, J. Sann, W. G. Zeier, J. Janek, *Chem. Mater.* **2016**, *28*, 2400.
[7] T. Krauskopf, H. Hartmann, W. G. Zeier, J. r. Janek, *ACS Appl. Mater. Interfaces* **2019**, *11*, 14463.
[8] J. A. Lewis, J. Tippens, F. J. Q. Cortes, M. T. McDowell, *Trends in Chemistry* **2019**, *1*, 845.
[9] Y.-K. Sun, *Meml. Serv. Exploit. Ind. Tab. Allumettes, Ser. B* **2020**, *5*, 3221.
[10] K. B. Hatzell, X. C. Chen, C. L. Cobb, N. P. Dasgupta, M. B. Dixit, L. E. Marbella, M. T. McDowell, P. P. Mukherjee, A. Verma, V. Viswanathan, A. S. Westover, W. G. Zeier, *ACS Energy Lett.* **2020**, *5*, 922.
[11] G. F. Dewald, S. Ohno, M. A. Kraft, R. Koerver, P. Till, N. M. Vargas-Barbosa, J. Janek, W. G. Zeier, *Chem. Mater.* **2019**, *31*, 8328.
[12] S. Wang, Q. Bai, A. M. Nolan, Y. Liu, S. Gong, Q. Sun, Y. Mo, *Angew. Chem., Int. Ed.* **2019**, *58*, 8039.
[13] A. Banerjee, X. Wang, C. Fang, E. A. Wu, Y. S. Meng, *Chem. Rev.* **2020**, *120*, 6878.
[14] L. M. Riegger, R. Schlem, J. Sann, W. G. Zeier, J. Janek, *Angew. Chem., Int. Ed.* **2021**, *60*, 6718.
[15] S. Wenzel, D. A. Weber, T. Leichtweiss, M. R. Busche, J. Sann, J. Janek, *Solid State Ionics* **2016**, *286*, 24.
[16] S. Wenzel, S. J. Sedlmaier, C. Dietrich, W. G. Zeier, J. Janek, *Solid State Ionics* **2018**, *318*, 102.
[17] S. Wenzel, T. Leichtweiss, D. Krüger, J. Sann, J. Janek, *Solid State Ionics* **2015**, *278*, 98.
[18] P. Hartmann, T. Leichtweiss, M. R. Busche, M. Schneider, M. Reich, J. Sann, P. Adelhelm, J. Janek, *J. Phys. Chem. C* **2013**, *117*, 21064.
[19] W. D. Richards, L. J. Miara, Y. Wang, J. C. Kim, G. Ceder, *Chem. Mater.* **2016**, *28*, 266.
[20] C. Hänsel, B. Singh, D. Kiwic, P. Canepa, D. Kundu, *Chem. Mater.* **2021**, *33*, 6029.
[21] J. A. Lewis, K. A. Cavallaro, Y. Liu, M. T. McDowell, *Joule* **2022**, *6*, 1418.
[22] S. Jin, Y. Ye, Y. Niu, Y. Xu, H. Jin, J. Wang, Z. Sun, A. Cao, X. Wu, Y. Luo, H. Ji, L.-J. Wan, *J. Am. Chem. Soc.* **2020**, *142*, 8818.
[23] J. He, Y. Wei, T. Zhai, H. Li, *Mater. Chem. Front.* **2018**, *2*, 437.
[24] D. H. S. Tan, Y.-T. Chen, H. Yang, W. Bao, B. Sreenarayanan, J.-M. Doux, W. Li, B. Lu, S.-Y. Ham, B. Sayahpour, J. Scharf, E. A. Wu, G. Deysher, H. E. Han, H. J. Hah, H. Jeong, J. B. Lee, Z. Chen, Y. S. Meng, *Science* **2021**, *373*, 1494.
[25] H. Pan, M. Zhang, Z. Cheng, H. Jiang, J. Yang, P. Wang, P. He, H. Zhou, *Sci. Adv.* **2022**, *8*, eabn4372.
[26] A. Santhosha, L. Medenbach, J. R. Buchheim, P. Adelhelm, *Batteries Supercaps* **2019**, *2*, 524.
[27] S. Luo, Z. Wang, X. Li, X. Liu, H. Wang, W. Ma, L. Zhang, L. Zhu, X. Zhang, *Nat. Commun.* **2021**, *12*, 6968.
[28] L. Zhou, T.-T. Zuo, C. Y. Kwok, S. Y. Kim, A. Assoud, Q. Zhang, J. Janek, L. F. Nazar, *Nat. Energy* **2022**, *7*, 83.
[29] T. Asano, A. Sakai, S. Ouchi, M. Sakaida, A. Miyazaki, S. Hasegawa, *Adv. Mater.* **2018**, *30*, 1803075.
[30] K.-H. Park, K. Kaup, A. Assoud, Q. Zhang, X. Wu, L. F. Nazar, *ACS Energy Lett.* **2020**, *5*, 533.
[31] S. Y. Kim, K. Kaup, K.-H. Park, A. Assoud, L. Zhou, J. Liu, X. Wu, L. F. Nazar, *ACS Mater. Lett.* **2021**, *3*, 930.
[32] S. Y. Kim, H. Cha, R. Kostecki, G. Chen, *ACS Energy Lett.* **2022**, *8*, 521.
[33] R. Court-Castagnet, C. Kaps, C. Cros, P. Hagenmuller, *Solid State Ionics* **1993**, *61*, 327.
[34] W. Ji, D. Zheng, X. Zhang, T. Ding, D. Qu, *J. Mater. Chem. A* **2021**, *9*, 15012.
[35] K. Kim, D. Park, H.-G. Jung, K. Y. Chung, J. H. Shim, B. C. Wood, S. Yu, *Chem. Mater.* **2021**, *33*, 3669.
[36] J. Fu, S. Wang, J. Liang, S. H. Alahakoon, D. Wu, J. Luo, H. Duan, S. Zhang, F. Zhao, W. Li, M. Li, X. Hao, X. Li, J. Chen, N. Chen, G. King, L.-Y. Chang, R. Li, Y. Huang, M. Gu, T.-K. Sham, Y. Mo, X. Sun, *J. Am. Chem. Soc.* **2022**, *145*, 2183.
[37] C. Rosenbach, F. Walther, J. Ruhl, M. Hartmann, T. A. Hendriks, S. Ohno, J. Janek, W. G. Zeier, *Adv. Energy Mater.* **2023**, *13*, 2203673.
[38] J. Liang, X. Li, S. Wang, K. R. Adair, W. Li, Y. Zhao, C. Wang, Y. Hu, L. Zhang, S. Zhao, S. Lu, H. Huang, R. Li, Y. Mo, X. Sun, *J. Am. Chem. Soc.* **2020**, *142*, 7012.
[39] J. Liang, E. van der Maas, J. Luo, X. Li, N. Chen, K. R. Adair, W. Li, J. Li, Y. Hu, J. Liu, L. Zhang, S. Zhao, S. Lu, J. Wang, H. Huang, W. Zhao, S. Parnell, R. I. Smith, S. Ganapathy, M. Wagemaker, X. Sun, *Adv. Energy Mater.* **2022**, *12*, 2103921.
[40] J. Li, A. R. Cameron, H. Li, S. Glazier, D. Xiong, M. Chatzidakis, J. Allen, G. A. Botton, J. R. Dahn, *J. Electrochem. Soc.* **2017**, *164*, A1534.

[41] X. Kong, Y. Zhang, S. Peng, J. Zeng, J. Zhao, *ACS Sustainable Chem. Eng.* **2020**, *8*, 14938.
[42] Y. Han, S. H. Jung, H. Kwak, S. Jun, H. H. Kwak, J. H. Lee, S.-T. Hong, Y. S. Jung, *Adv. Energy Mater.* **2021**, *11*, 2100126.
[43] C. Wang, R. Yu, S. Hwang, J. Liang, X. Li, C. Zhao, Y. Sun, J. Wang, N. Holmes, R. Li, *Energy Storage Mater.* **2020**, *30*, 98.
[44] I. Kochetkov, T.-T. Zuo, R. Ruess, B. Singh, L. Zhou, K. Kaup, J. Janek, L. Nazar, *Energy Environ. Sci.* **2022**, *15*, 3933.
[45] X. Li, J. Liang, K. R. Adair, J. Li, W. Li, F. Zhao, Y. Hu, T.-K. Sham, L. Zhang, S. Zhao, S. Lu, H. Huang, R. Li, N. Chen, X. Sun, *Nano Lett.* **2020**, *20*, 4384.
[46] X. Li, J. Liang, J. Luo, M. N. Banis, C. Wang, W. Li, S. Deng, C. Yu, F. Zhao, Y. Hu, T. Sham, L. Zhang, S. Zhao, S. Lu, H. Huang, R. Li, K. R. Adaira, X. Sun, *Energy Environ. Sci.* **2019**, *12*, 2665.
[47] B. Hedman, K. O. Hodgson, E. I. Solomon, *J. Am. Chem. Soc.* **1990**, *112*, 1643.
[48] A. Rompel, J. C. Andrews, R. M. Cinco, M. W. Wemple, G. Christou, N. A. Law, V. L. Pecoraro, K. Sauer, V. K. Yachandra, M. P. Klein, *J. Am. Chem. Soc.* **1997**, *119*, 4465.
[49] M. W. Löble, J. M. Keith, A. B. Altman, S. C. E. Stieber, E. R. Batista, K. S. Boland, S. D. Conradson, D. L. Clark, J. Lezama Pacheco, S. A. Kozimor, R. L. Martin, S. G. Minasian, A. C. Olson, B. L. Scott, D. K. Shuh, T. Tyliszczak, M. P. Wilkerson, R. A. Zehnder, *J. Am. Chem. Soc.* **2015**, *137*, 2506.
[50] L. Fan, H. L. Zhuang, K. Zhang, V. R. Cooper, Q. Li, Y. Lu, *Adv. Sci.* **2016**, *3*, 1600175.
[51] Y. Lu, C.-Z. Zhao, R. Zhang, H. Yuan, L.-P. Hou, Z.-H. Fu, X. Chen, J.-Q. Huang, Q. Zhang, *Sci. Adv.* **2021**, *7*, eabi5520sss.
[52] R. Schlem, A. Banik, S. Ohno, E. Suard, W. G. Zeier, *Chem. Mater.* **2021**, *33*, 327.
[53] T. K. Schwietert, V. A. Arszelewska, C. Wang, C. Yu, A. Vasileiadis, N. J. J. de Klerk, J. Hageman, T. Hupfer, I. Kerkamm, Y. Xu, E. van der Maas, E. M. Kelder, S. Ganapathy, M. Wagemaker, *Nat. Mater.* **2020**, *19*, 428.
[54] L. Gao, Y. Xie, Y. Tong, M. Xu, J. You, H. Wei, X. Yu, S. Xu, Y. Zhang, Y. Che, *Sci. China Technol. Sci.* **2023**, 66, 2059.
[55] Z. Siroma, T. Sato, T. Takeuchi, R. Nagai, A. Ota, T. Ioroi, *J. Power Sources* **2016**, *316*, 215.
[56] P. Vadhva, J. Hu, M. J. Johnson, R. Stocker, M. Braglia, D. J. Brett, A. J. Rettie, *ChemElectroChem* **2021**, *8*, 1930.
[57] S. Wang, W. Zhang, X. Chen, D. Das, R. Ruess, A. Gautam, F. Walther, S. Ohno, R. Koerver, Q. Zhang, W. G. Zeier, F. H. Richter, C.-W. Nan, J. Janek, *Adv. Energy Mater.* **2021**, *11*, 2100654.
[58] I. V. Krasnikova, M. A. Pogosova, A. O. Sanin, K. J. Stevenson, *Chem. Mater.* **2020**, *32*, 2232.
[59] Z. Rong, R. Malik, P. Canepa, G. Sai Gautam, M. Liu, A. Jain, K. Persson, G. Ceder, *Chem. Mater.* **2015**, *27*, 6016.
[60] L. E. Blanc, Y. Choi, A. Shyamsunder, B. Key, S. H. Lapidus, C. Li, L. Yin, X. Li, B. Gwalani, Y. Xiao, C. J. Bartel, G. Ceder, L. F. Nazar, *Chem. Mater.* **2023**, *35*, 468.
[61] L. Yin, B. J. Kwon, Y. Choi, C. J. Bartel, M. Yang, C. Liao, B. Key, G. Ceder, S. H. Lapidus, *J. Am. Chem. Soc.* **2021**, *143*, 10649.
[62] F. Maroni, S. Dongmo, C. Gauckler, M. Marinaro, M. Wohlfahrt-Mehrens, *Batteries Supercaps* **2021**, *4*, 1221.
[63] F. Han, A. S. Westover, J. Yue, X. Fan, F. Wang, M. Chi, D. N. Leonard, N. J. Dudney, H. Wang, C. Wang, *Nat. Energy* **2019**, *4*, 187.
[64] S. Webb, *Phys. Scr.* **2005**, *2005*, 1011.
[65] S. Webb, in AIP Conference Proceedings, American Institute of Physics, MD, **2005**, pp.196–199.
[66] N. Tamura, M. Kunz, K. Chen, R. S. Celestre, A. A. MacDowell, T. Warwick, *Mater. Sci. Eng., A* **2009**, *524*, 28.
[67] R. Schlem, S. Muy, N. Prinz, A. Banik, Y. Shao-Horn, M. Zobel, W. G. Zeier, *Adv. Energy Mater.* **2020**, *10*, 1903719.
[68] S. P. Ong, W. D. Richards, A. Jain, G. Hautier, M. Kocher, S. Cholia, D. Gunter, V. L. Chevrier, K. A. Persson, G. Ceder, *Comput. Mater. Sci.* **2013**, *68*, 314.
[69] G. Kresse, J. Furthmüller, *Phys. Rev. B* **1996**, *54*, 11169.
[70] P. E. Blöchl, *Phys. Rev. B* **1994**, *50*, 17953.
[71] J. P. Perdew, K. Burke, M. Ernzerhof, *Phys Rev Lett* **1996**, *77*, 3865.
[72] A. Jain, S. P. Ong, G. Hautier, W. Chen, W. D. Richards, S. Dacek, S. Cholia, D. Gunter, D. Skinner, G. Ceder, K. A. Persson, *APL Mater.* **2013**, 1, 011002.
[73] R. Bruce, M. Newville, *J. Synchrotron. Radiat.* **2005**, *12*, 537.